Spatiotemporal Evolution of Runaway Electron Momentum Distributions in Tokamaks

C. Paz-Soldan, C. M. Cooper, P. Aleynikov, D. C. Pace, N. W. Eidietis, D. P. Brennan, R. S. Granetz, E. M. Hollmann, C. Liu, A. Lvovskiy, R. A. Moyer, and D. Shiraki

Phys. Rev. Lett. **118**, 255002 — Published 22 June 2017

DOI: 10.1103/PhysRevLett.118.255002

Spatio-temporal Evolution of Runaway Electron Momentum Distributions in Tokamaks

C. Paz-Soldan,[1,*] C. M. Cooper,[2] P. Aleynikov,[3] D. C. Pace,[1] N. W. Eidietis,[1] D. P. Brennan,[4] R. S. Granetz,[5] E. M. Hollmann,[6] C. Liu,[4] A. Lvovskiy,[2] R. A. Moyer,[6] and D. Shiraki[7]
[1] *General Atomics, San Diego, CA, USA*
[2] *Oak Ridge Associated Universities, Oak Ridge, TN, USA*
[3] *Max-Planck Institute for Plasma Physics, Greifswald, Germany*
[4] *Princeton University, Princeton, NJ, USA*
[5] *Massachusetts Institute of Technology, Cambridge MA, USA*
[6] *University of California-San Diego, La Jolla, CA, USA*
[7] *Oak Ridge National Laboratory, Oak Ridge, TN, USA*
(Dated: May 3, 2017)

Novel spatial, temporal, and energetically resolved measurements of bremsstrahlung hard X-ray (HXR) emission from runaway electron (RE) populations in tokamaks reveal non-monotonic RE distribution functions whose properties depend on the interplay of electric field acceleration with collisional and synchrotron damping. Measurements are consistent with theoretical predictions of momentum-space attractors that accumulate runaway electrons. RE distribution functions are measured to shift to higher energy when the synchrotron force is reduced by decreasing toroidal magnetic field strength. Increasing collisional damping by increasing electron density (at fixed magnetic and electric field) reduces the energy of the non-monotonic feature and reduces the HXR growth rate at all energies. Higher energy HXR growth rates extrapolate to zero at the expected threshold electric field for RE sustainment while low energy REs are anomalously lost. Compilation of HXR emission from different sight-lines into the plasma yields energy and pitch-angle resolved RE distributions and demonstrates increasing pitch-angle and radial gradients with energy.

PACS numbers: 52.30.Cv, 52.20.Fs, 52.25.Dg, 52.55.Fa, 52.40.Mj

Introduction Reaching mega-ampere currents and mega-electron volt (MeV) energies during fast shutdown events, runaway electrons (REs) pose perhaps the greatest operational risk to tokamak fusion reactors such as ITER [1–4]. Due to the severe potential for damage to the reactor walls, opportunities for empirical tuning of RE control actuators will be limited. Instead, a first-principles predictive understanding is needed, and present-day experiments fill a crucial need in validating theoretical predictions of RE dissipation.

Classical theories for relativistic RE generation in tokamaks based on the effects of Coulomb collisions (small angle [5] and secondary avalanche [6]) determine the critical electric field (E_{C}) for the growth of RE populations. Further work highlighted the important role of synchrotron damping in elevating the threshold electric field above E_{C} [7, 8], and several experiments have since yielded evidence of the elevated threshold [9–12]. These observations motivated the development of a rigorous analytical theory [13] and computational tools [14–19] that clarified the importance of the effects of pitch-angle scattering and synchrotron damping. Alongside quantifying the enhancement of the threshold field, these works predict phase-space circulation around an attractor resulting in a pile-up of REs at specific energies potentially resulting in non-monotonic features in the RE distribution function (f_e). While important to the RE dissipation rate and thus the prospects for control, neither have these features of f_e been directly observed nor has a detailed model validation of experimental f_e together with dissipation rates been made until now.

In this Letter we report the first spatially, energetically, and temporally resolved reconstructions of f_e in tokamaks and their dependence on plasma parameters. The effect of varying synchrotron and collisional damping on f_e is directly shown and direct comparisons to time-dependent modeling are made. This significantly expands on previous measurements [20–22] by spatially localizing the RE emission, isolating the synchrotron effect, and comparing directly to modeling. Experiments are conducted using trace RE populations in low-density Ohmic plasmas [11] in the DIII-D tokamak with parameters targeted to non-dimensionally match the expected conditions in post-disruption RE beams in ITER, with both predicted to develop non-monotonic f_e. Non-monotonic features at the predicted energies are observed and their dependence on synchrotron and collisional damping rates will be described.

Measurement Technique Emission from RE populations are measured using a novel toroidally-viewing (tangential) pinhole camera made entirely of lead, pictured in Fig. 1(a) and described in detail in Refs. [23, 24]. Bremsstrahlung radiation emitted when a RE scatters off a plasma ion or neutral is collimated into the discrete sight-lines of the camera. Due to the tangential view only emission from low pitch-angle REs is measured. The sight-lines view different parts of the plasma cross-section, shown in Fig. 1(b). Along each sight-line, differ-

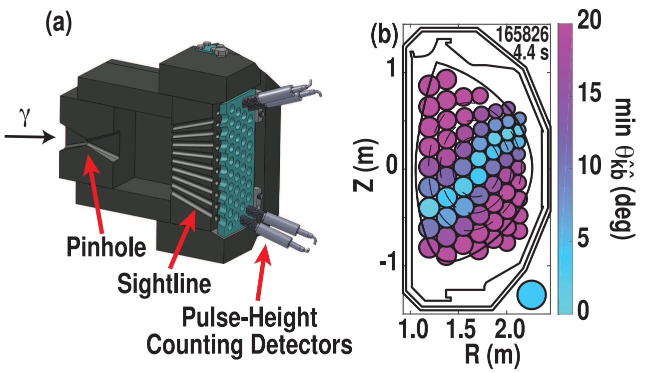

FIG. 1. (a) Lead pinhole camera geometry and (b) sight-lines into the plasma at the tangency plane. Colors indicate the minimum angle ($\theta_{\hat{k}\hat{b}}$) between the magnetic field orientation ($\hat{b}$) and the sight-line orientation ($\hat{k}$). The lower-right circle in (b) denotes a full-view sightline.

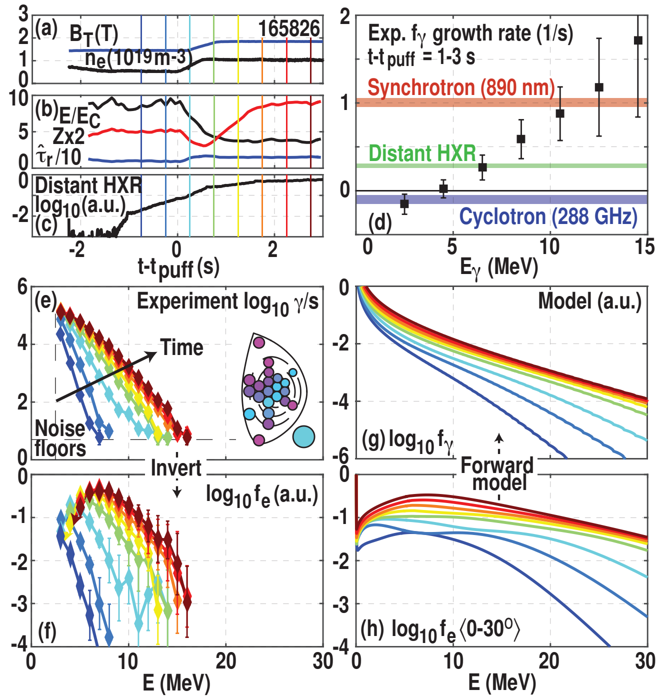

FIG. 2. (a) Experimental actuators, (b) non-dimensional parameters, and (c) distant HXR signal for a typical discharge. (d-e) measured f_γ shows increasing growth rate as energy increases, and flattening at mid-energy consistent with (f) non-monotonic f_e feature formation. (g-h) Model predictions of f_γ and f_e are broadly consistent with the data.

ent angles are made between the equilibrium magnetic field direction ($\hat{b}$, obtained from equilibrium reconstructions) and the sight-line orientation ($\hat{k}$). The minimum $\theta_{\hat{k}\hat{b}}$ along the sight-line is used to color code the view. Emission along each active sight-line is measured by a Bismuth-Germanate (BGO) scintillating crystal together with a photodiode. The scintillation pulses from individual photons are digitized at 10 MHz sample rate, with the pulse height determining the photon energy (E_γ). Binning the pulse heights in time allows an energy spectrum of HXR photons (f_γ) to be assembled. f_γ is a convolution of f_e, the bremsstrahlung emission coefficients [25], and Compton scattering in the scintillator [26]. Assuming spatial homogeneity of f_e, knowledge of the bremsstrahlung emission and Compton scattering allows inversion of f_γ to f_e by computing the expected f_γ from a set of mono-energetic f_e. In the inversions finite pitch-angle effects are ignored thus only 1-D experimental f_e are shown.

Background Plasma and Modeling Framework The quiescent flat-top scenario is employed [11]. Initial low density operation builds a robust (and monotonic) RE population due to primary (Dreicer) production that also undergoes secondary avalanche. When the REs reach a critical intensity, an asynchronous trigger at $t_{\rm puff}$ begins the RE dissipation phase. Here, background plasma properties such as the toroidal magnetic field (B_T) and the electron density (n_e) are actuated independently [shown in Fig. 2(a)] to vary the RE damping terms and study their effect on f_e. Primary production ceases in the dissipation phase as thermal transport changes reduce the electron temperature. Note the dimensional B_T and n_e map to changes in the synchrotron and collisional damping terms, and are non-dimensionalized by the parameters $\hat{\tau}_{\rm r}$ ($\equiv \frac{3}{2}\left(\frac{m_e \ln\Lambda}{\epsilon_0}\right)\frac{n_e}{B_T^2} \approx 28\frac{n_e[10^{19}{\rm m}^{-3}]}{(B_T[{\rm T}])^2}$, the ratio of the collision to the synchrotron damping time), and $E/E_{\rm C}$ ($\equiv \frac{4\pi\varepsilon_0^2 m_e V_C^2}{n_e e^3 \ln\Lambda} \approx 10\frac{V_{\rm loop}[{\rm V}]}{n_e[10^{19}{\rm m}^{-3}]}$, the ratio of the toroidal electric field to the critical field). E is measured at the plasma surface but any radial gradients relax quickly ($<$ 1 s) compared to discharge time scales. The ion charge Z is also measured with charge exchange spectroscopy and actuated by replacing deuterium ions (Z=1) with nitrogen ions (Z=7) holding n_e constant. The plasma retains keV thermal temperatures and is thus fully ionized, so no corrections due to bound electrons are needed. The non-dimensional $E/E_{\rm C}$, Z, and $\hat{\tau}_{\rm r}$ accessed are similar to expected values in ITER thus giving access to ITER-relevant RE dissipation regimes.

To model the evolution of f_e the time-dependent relativistic 2D Fokker-Planck equation (ex. Ref. [27]) is solved numerically inputting measured on-axis (spatially 0-D) plasma parameters [Fig. 2(b)]. The equation as in Ref. [13] is solved with two amendments: 1) the collision operator is extended to be valid for lower energies (similar to Refs. [28, 29]) and 2) an approximate secondary source is included which captures the effect of a finite energy incident electron population. This treatment accurately captures the analytical results of RE generation models [5, 6, 30] as well as the near-threshold regime [13]. The computed f_e evolution is then placed through a forward model taking into account bremsstrahlung emission coefficients and sight-line geometry to obtain the predicted f_γ [24]. Unlike inversion from f_γ to f_e, forward modeling from f_e to f_γ requires no assumptions, though in accordance with the tangential view only the low pitch-angle part of the distribution ⟨0-30°⟩ is used in the f_γ calculation (though taken to have zero pitch-angle).

Global Distribution Measurement The discharge in Fig. 2 accesses strong synchrotron damping ($\hat{\tau}_r \approx 15$), high Z (≈ 4), and modest collisional damping ($E/E_C \approx 4$) [Fig. 2(a,b)]. For these parameters, the total HXR energy flux measured on a distant plastic scintillator [Bicron BC-400, Fig. 2(c)] grows. Measurements (here aggregating all spatial channels) find very different f_γ growth rates with HXR energy (E_γ) [Fig. 2(d)]. Comparison of growth rates across emission bands are consistent. At low E_γ ($\leq$2 MeV), f_γ decays together with 288 GHz electron cyclotron emission (ECE), as expected since ECE is dominated by low energy REs. Similarly, high E_γ growth rates match that of visible synchrotron emission (SE) at 890 nm, as expected since SE is dominated by high-energy (>10 MeV) REs [31]. The growth rate of the distant HXR detector is skewed to low E_γ, indicating that this type of diagnostic (often used to infer RE population) does not clearly discriminate between RE energy and population.

Measurements of f_γ and inversion to f_e [Fig. 2(e,f)] reveal f_γ changes at mid-energy which upon inversion map to the development of a non-monotonic f_e from an originally peaked f_e. Modeling of this same discharge to predict f_e and forward model f_γ [Fig. 2(g,h)] indicates a similar evolution is predicted. As with experiment, f_γ increases more rapidly at high energy, and a non-monotonic feature in f_e is computed for these experimental conditions at a similar energy ($\approx$ 7 MeV). The final f_e shape is near-stationary, indicating the phase-space circulation effect gives rise to the non-monotonic feature. Note the absence of f_e points late in time below 5 MeV is due to the prediction of slightly negative f_e (with large uncertainty) due to the subtractions involved in the inversion process, indicating that while the degree of hollowness is difficult to quantify, peaked f_e are excluded. Additionally, two experimental noise floors are present: at low flux due to limited counting statistics ($\leq 5\gamma/s$), and at low energy due to pulse heights approaching electronic noise levels ($\leq$ 1 MeV). Modeled f_e are momentum-space distributions plotted against energy, normalized by $n_{RE} = \int f_e dp$, and take units [γ/MeV s]. While normalization affects the f_e shape, this normalization follows directly from experiment (γ/s count rate histograms with uniform 1 MeV binning) and also highlights attractor dynamics.

Angular and Spatial Dependencies Comparison of f_γ from individual sight-lines allows extraction of radial and pitch-angle profiles of sufficiently energetic REs. This is due to the angular localization of bremsstrahlung emission provided by the relativistic forward-beaming effect. Assuming f_e decreases with pitch angle, emission into a sight-line with a small minimum $\theta_{\hat{k}\hat{b}}$ will be dominated by small pitch angle REs. In contrast, emission into sight-lines with large minimum $\theta_{\hat{k}\hat{b}}$ will predominantly

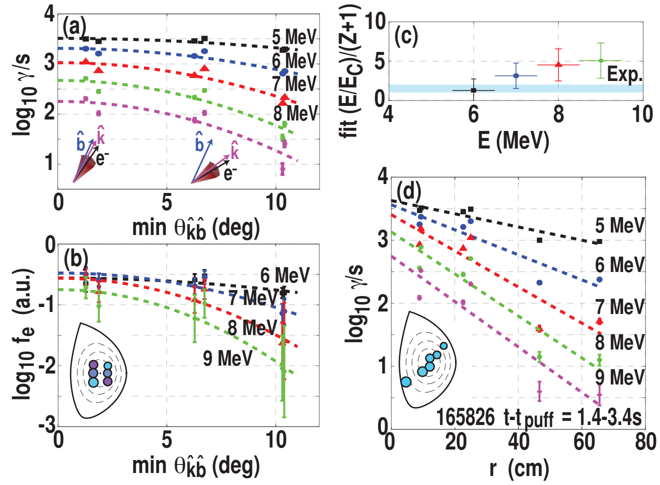

FIG. 3. Angular and spatial RE distribution dependency for the same discharge of Fig. 2. Experimental (a-b) f_γ and f_e show reductions at high $\theta_{\hat{k}\hat{b}}$, allowing (c) inference of E/E_C to (Z+1) according to Ref. [13]. (d) Energy-dependent f_γ radial falloff is also observed.

see REs whose pitch angle roughly matches $\theta_{\hat{k}\hat{b}}$. Contributions from larger $\theta_{\hat{k}\hat{b}}$ points along any sightline are weaker as f_e (and thus emission) decreases with pitch angle. Measurement geometry is further described in Ref. [24]. Thus, comparing f_γ from sight-lines viewing the same flux surface at different minimum $\theta_{\hat{k}\hat{b}}$ is roughly equivalent to resolving the f_γ pitch-angle distribution. An example pitch-angle resolved f_γ measurement is shown in Fig. 3(a), plotting against the minimum $\theta_{\hat{k}\hat{b}}$ and illustrating energy-dependent fall-off. Note 10 MeV emission cones are narrower than minimum $\theta_{\hat{k}\hat{b}}$ separation (see cartoon), though blurring does occur below 5 MeV, setting a low E_γ angular resolution limit. f_γ from each sight-line can be inverted [Fig. 3(b)], confirming expectations of a more forward beamed f_e at higher energy. The inferred f_e pitch-angle dependence can be compared to theoretical predictions [13] of exponential angle fall-off with a decay coefficient proportional to the ratio of E/E_C to $Z+1$. As shown in Fig. 3(c), the prediction is within experimental uncertainty below 7 MeV. At higher energy f_e is more forward beamed than expected for reasons that are not yet understood, though uncertainties are larger for this measurement due to lower the counting statistics of single sight-lines. Improving counting statistics through repeat discharges or increased detector efficiency will reduce uncertainty at high E_γ, allowing for example the formulation of Ref. [8] to be validated. Future work will also pursue 2-D (angle-resolved) f_e inversions.

Individual sight-lines with the same low minimum $\theta_{\hat{k}\hat{b}}$ but viewing different flux surfaces can also be used to measure radial profiles of f_γ, as shown in Fig. 3(d). As with the pitch-angle distribution, radial fall-off is more pronounced at high energy, indicating energy-dependent spatial transport is present.

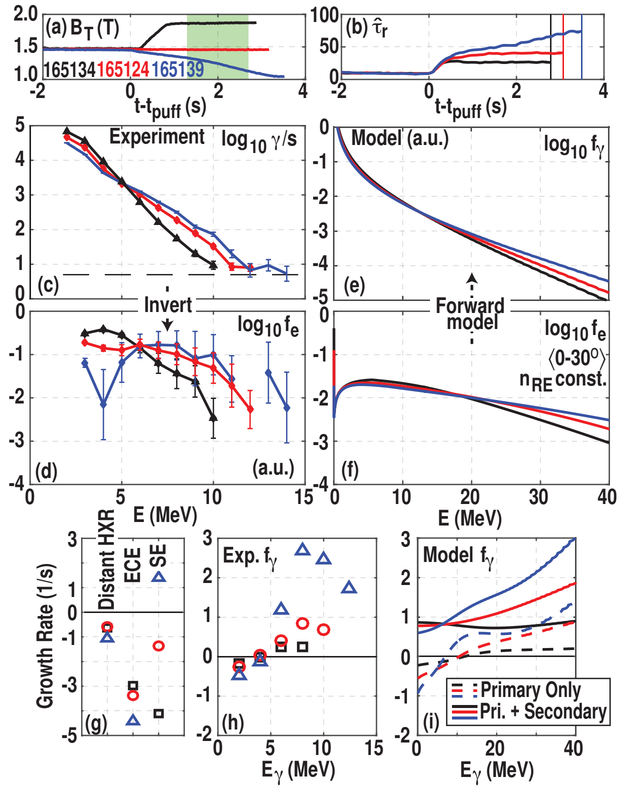

FIG. 4. Effect of modifying synchrotron force on RE distributions actuated through (a) varying the toroidal field (B_T) resulting in a wide change in $\hat{\tau}_\mathrm{r}$ (b). Measured (c) f_γ and (d) f_e from the green interval in (a) show an expansion to high energy and contraction at low energy. Model (e) f_γ and (f) f_e show qualitative similarity (note different energy scale), normalizing to constant n_{RE}. Growth rate analysis for (g) other diagnostics, (h) experimental f_γ, and (i) model f_γ are also shown.

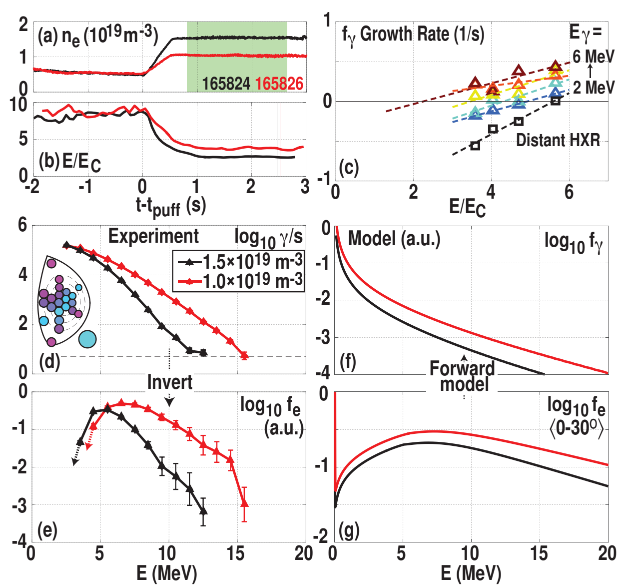

FIG. 5. Effect of modifying collisional damping by increasing (a) n_e resulting in (b) a decrease in E/E_C. Measured (c) f_γ and (d) f_e from the green interval in (a) indicate that RE energization is inhibited, consistent with model predicted (e) f_γ and (f) f_e. (g) f_γ growth rates indicate high-energy REs decay at a lower E/E_C than low energy REs.

Global Parametric Dependencies Modifying the synchrotron and collisional damping rate is found to have a strong effect on the measured f_γ and f_e in both theory and experiment (aggregating now over all active sight-lines). The effect of synchrotron radiation is isolated by using three matched discharges with similar prehistories and post-puff parameters ($E/E_\mathrm{C} = 3.1\pm0.3$ and $Z = 1.4 \pm 0.1$) but varying B_T, thus accessing a wide range of $\hat{\tau}_\mathrm{r}$ [Fig. 4(a-b)]. Experimental f_γ [Fig. 4(c)] demonstrate a reduction in high E_γ counts and an increased spectral index as B_T is raised, opposite to the expectation from single-particle confinement arguments, yet consistent with synchrotron effects limiting the high-energy f_e. Interestingly, at low E_γ a decrease in f_γ is found with decreasing B_T. Experimental f_e [Fig. 4(d)] indicates the RE distribution is getting progressively flatter as B_T is decreased, with the lowest B_T displaying a non-monotonic feature in f_e outside of experimental uncertainty. Modeling of these cases [Fig. 4(e-f)] qualitatively predicts the observed shape variations with $\hat{\tau}_\mathrm{r}$. However, variations between f_e and f_γ at different $\hat{\tau}_\mathrm{r}$ are observed at lower energy than in modeling, indicating a stronger B_T effect in experiment potentially due to the neglect of spatial effects. Indeed, the input on-axis B_T value is lower than the inboard value, which is also where visible synchrotron emission is known to be localized [11, 31].

Considering emission growth rates [Fig. 4(g,h)] the distant HXR, ECE, and low E_γ f_γ growth rates all decrease with increasing B_T. In contrast, SE and high E_γ f_γ rates display the opposite B_T trend. All emissions are thus broadly consistent a shift to high energy as B_T is lowered. Note however quantitative ECE and SE growth rates differ from the f_γ rates, due to the direct B_T dependencies of these emissions. The corresponding model-predicted f_γ growth rates are shown in Fig. 4(i). Agreement is good at high E_γ, though at low E_γ the observed decay is not reproduced unless the secondary source term is artificially removed as might be expected if E/E_C were somewhat lower.

Increasing collisional damping by raising n_e thus decreasing E/E_C [Fig. 5(a-b)] is found to decrease the growth rate of HXR emission [Fig. 5(c)] across all E_γ. Growth rates of all other measured emissions (ECE, SE, distant HXR) also decrease as E/E_C is reduced (not shown). A transition from HXR signal growth to decay at E/E_C far above E/E_C=1 is measured on the distant plastic scintillator (as reported in Refs. [11, 12]) but the E_γ dependence of this diagnostic is unclear. E_γ resolved measurements reveal increasing HXR growth rate with E_γ at fixed E/E_C [also seen in Fig. 4(h)]. Thus, the E/E_C value where HXR growth transitions to decay decreases with increasing E_γ. While extrapolation is necessary to find this value at high energy, it is roughly at $E/E_\mathrm{C} \approx 2$. This compares more favorably to the threshold field for RE generation which is predicted to be at E/E_C=1.6 for these conditions [13], indicating a more consistent behavior at high energy. Comparison of experimental and model f_γ and f_e [Fig. 5(d-g)] show good agreement, with the high E/E_C case extending to higher energy and with a harder spectral index than at low E/E_C. The experimental non-monotonic feature increases in energy from 5 to 7 MeV as E/E_C is raised, also in good agreement with model predictions (from 6 to 7 MeV).

Summary and Conclusion Comparing experimental and modeled f_e, nearly all qualitative trends are captured: 1) both develop non-monotonic features at consistent energy, 2) f_e are more parallel-directed at high energy, 3) increasing synchrotron damping (lowering $\hat{\tau}_r$) shifts f_e towards lower energy, 4) increasing collisional damping (lowering E/E_C) decreases f_e at all energies. The f_e shape and location of non-monotonic features are generally in agreement as E/E_C and $\hat{\tau}_r$ are varied.

An exception to the wide qualitative agreement between experiment and theory is the behavior at low energy, where systematically lower f_γ growth rates are observed. The cause remains unknown, but may be due to spatial transport effects not included in the 0-D model [32]. Allowing for momentum-dependent spatial diffusion (as expected from magnetic fluctuations) also introduces free parameters to fit the observed spatial f_e trends, but does not exclude other mechanisms (such as kinetic instability due to f_e shape) from impacting the spatial gradients. Other spatial effects, such as an increase of the calculated synchrotron damping under a full-orbit treatment [33], may also contribute to explaining the quantitatively stronger effect of B_T seen in experiment.

To conclude, novel measurements provide first confirmation of non-monotonic features in RE distribution functions and their dependence on collisional and synchrotron damping terms. The broad agreement found validates the importance of these effects and improves confidence that these models can be used to design optimized RE mitigation strategies. Looking forward, the identified discrepancies will guide improvements to RE dissipation models and enable improved validation against the spatial, temporal, pitch-angle, and energetic effects described herein.

DIII-D data shown in this paper can be obtained in digital format by following the links at `https://fusion.gat.com/global/D3D_DMP`. The authors thank M. Austin, S. Haskey, B. Grierson, and Y. Zhu for diagnostic support, as well as N. Commaux, and A. Wingen for their assistance, and T. Fülöp, O. Embréus, A. Stahl, and G. Wilkie for useful discussions. This material is based upon work supported in part by the U.S. Department of Energy under Grants DE-FC02-04ER54698, DE-FG02-07ER54917, DE-AC05-00OR22725, DE-FC02-99ER54512, DE-SC0016268.

* paz-soldan@fusion.gat.com

[1] T. C. Hender et. al, Nucl. Fusion **47**, S128 (2007).
[2] M. Lehnen et. al, J. of Nucl. Mat. 463 39-48 (2014).
[3] E. M. Hollmann et. al, Phys. Plasmas **22**, 021802 (2015).
[4] A. H. Boozer, Phys. of Plasmas **22** (2015).
[5] J. Connor and R. Hastie, Nucl. Fusion **15**, 415 (1975).
[6] M. N. Rosenbluth and S. V. Putvinski, Nucl. Fusion **37**, 1355 (1997).
[7] J. R. Martin-Solis, J. D. Alvarez, R. Sanchez, and B. Esposito, Phys. of Plasmas **5**, 2370 (1998).
[8] F. Andersson, P. Helander, and L. G. Eriksson, Phys. Plasmas **8**, 5221 (2001).
[9] J. R. Martin-Solis, R. Sánchez, and B. Esposito, Phys. Rev. Lett. **105**, 185002 (2010).
[10] E. M. Hollmann et. al,Nucl. Fusion **51**, 103026 (2011).
[11] C. Paz-Soldan, N. W. Eidietis, R. S. Granetz, E. M. Hollmann, R. A. Moyer, N. A. Crocker, A. Wingen, and Y. Zhu, Phys. Plasmas **21**, 022514 (2014).
[12] R. S. Granetz, B. Esposito, J. H. Kim, R. Koslowski, M. Lehnen, J. R. Martin-Solis, C. Paz-Soldan, T. Rhee, J. C. Wesley, L. Zeng, and the ITPA MHD Group, Phys. Plasmas **21**, 072506 (2014).
[13] P. B. Aleynikov and B. N. Breizman, Phys. Rev. Lett. **114**, 155001 (2015).
[14] P. B. Aleynikov, K. Aleynikova, B. N. Breizman, G. T. A. Huijsmans, S. V. Konovalov, S. V. Putvinski, and V. Zhogolev, in *Proc. of 25th IAEA Fusion Energy Conf. (St. Petersburg, Russia)* (2014) pp. TH/P3–38.
[15] E. Hirvijoki, I. Pusztai, J. Decker, O. Embréus, A. Stahl, and T. Fülöp, J. Plasma Phys. **81**, 475810502 (2015).
[16] A. Stahl, E. Hirvijoki, J. Decker, O. Embréus, and T. Fülöp, Phys. Rev. Lett. **114**, 115002 (2015).
[17] C. Liu, D. P. Brennan, A. H. Boozer, and A. Bhattacharjee, Phys. Plasmas **23**, 010702 (2015).
[18] J. Decker, E. Hirvijoki, O. Embréus, Y. Peysson, A. Stahl, I. Pusztai, and T. Fülöp, Plasma Phys. Contr. Fusion **58**, 025016 (2016).
[19] C. Liu, D. P. Brennan, A. H. Boozer, A. Bhattacharjee, Plasma Phys. Contr. Fusion **59**, 024003 (2017).
[20] A. E. Shevelev, E. M. Khilkevitch, V. G. Kiptily, I. N. Chugunov, D. B. Gin, D. N. Doinikov, V. O. Naidenov, A. E. Litvinov, and I. A. Polunovskii, Nucl. Fusion **53**, 123004 (2013).
[21] A. E. Shevelev, E. M. Khilkevitch, S. I. Lashkul, V. V. Rozhdestvensky, and A. B. Altukhov, Nucl. Instrum. Methods Phys. Res., Sect. A **830**, 102 (2016).
[22] E. M. Hollmann, P. B. Parks, N. Commaux, N. W. Eidietis, R. A. Moyer, D. Shiraki, M. E. Austin, C. J. Lasnier, C. Paz-Soldan, and D. L. Rudakov, Phys. Plasmas **22**, 056108 (2015).
[23] D. C. Pace, C. M. Cooper, D. Taussig, N. W. Eidietis, E. M. Hollmann, V. Riso, and M. A. Van Zeeland, Rev. Sci. Instrum. **87**, 043507 (2016).
[24] C. M. Cooper, D. C. Pace, N. Commaux, N. W. Eidietis, E. M. Hollmann, and D. Shiraki, Rev. Sci. Instrum. **87**, 11E602 (2016).
[25] H. W. Koch and J. W. Motz, Rev. Mod. Phys. **31**, 920 (1959).
[26] Y. Peysson and F. Imbeaux, Rev. Sci. Instrum. **70**, 3987 (1999).

[27] L.-G. Eriksson and P. Helander, Comput. Phys. Commun. **154**, 175 (2003).
[28] P. Helander, *Collisional Transport in Magnetized Plasmas* (Cambridge University Press, 2002).
[29] G. Papp, M. Drevlak, T. Fülöp, and P. Helander, Nucl. Fusion **51**, 43004 (2011).
[30] P. B. Parks, M. Rosenbluth, and S. Putvinski, Phys. Plasmas **6** (1999).
[31] J. H. Yu, E. M. Hollmann, N. Commaux, N. W. Eidietis, D. A. Humphreys, A. N. James, T. C. Jernigan, and R. A. Moyer, Phys. Plasmas **20**, 042113 (2013).
[32] P. Helander, L.-G. Eriksson, and F. Andersson, Phys. Plasmas **7**, 4106 (2000).
[33] L. Carbajal, D. Del-Castillo-Negrete, D. Spong, S. Seal, and L. Baylor, Physics of Plasmas **24**, 042512 (2017).